NEOPLASIA
www.neoplasia.com

Volume 18 Number 8 August 2016 pp. 459–467 459

High-Resolution Multispectral Optoacoustic Tomography of the Vascularization and Constitutive Hypoxemia of Cancerous Tumors[1]

Andrei Chekkoury*,†,2, Antonio Nunes*,2, Jerome Gateau*,†,§, Panagiotis Symvoulidis*,†, Annette Feuchtinger‡, Nicolas Beziere*, Saak V. Ovsepian*,†, Axel Walch‡ and Vasilis Ntziachristos*,†

*Institute for Biological and Medical Imaging, Helmholtz Zentrum München, Deutsches Forschungszentrum für Gesundheit und Umwelt (GmbH), Ingolstädter Landstr., 85764 Neuherberg, Germany; †Munich School of Bioengineering, Technische Universität München (TUM), Ismaningerstr. 22, 81675 München, Germany; ‡Research Unit of Analytical Pathology, Institute of Pathology, Helmholtz Zentrum München, Ingolstädter Landstr. 1, 85764 Neuherberg, Germany; §ESPCI Paris-Tech, PSL Research University, CNRS, Institut Langevin, 1 rue Jussieu, F-75005, Paris, France

Abstract

Diversity of the design and alignment of illumination and ultrasonic transducers empower the fine scalability and versatility of optoacoustic imaging. In this study, we implement an innovative high-resolution optoacoustic mesoscopy for imaging the vasculature and tissue oxygenation within subcutaneous and orthotopic cancerous implants of mice *in vivo* through acquisition of tomographic projections over 180° at a central frequency of 24 MHz. High-resolution volumetric imaging was combined with multispectral functional measurements to resolve the exquisite inner structure and vascularization of the entire tumor mass using endogenous and exogenous optoacoustic contrast. Evidence is presented for constitutive hypoxemia within the carcinogenic tissue through analysis of the hemoglobin absorption spectra and distribution. Morphometric readouts obtained with optoacoustic mesoscopy have been verified with high-resolution ultramicroscopic studies. The findings described herein greatly extend the applications of optoacoustic mesoscopy toward structural and multispectral functional measurements of the vascularization and hemodynamics within solid tumors *in vivo* and are of major relevance to basic and preclinical oncological studies in small animal models.

Neoplasia (2016) 18, 459–467

Introduction

Angiogenesis is a principal hallmark of malignant tumors and has been implicated as a therapeutic target [1,2]. In the course of carcinogenesis, nascent vessels feeding growing tumors have been reported to become irregular, acquire tortuous shape, and develop profuse system of anastomoses, resulting in atypical vascularization of the tissue mass with focal hypoxia and occasional bleeding [3,4]. Hence, imaging of the vasculature and hemoglobin gradients in tumors can reveal its malignant features, facilitating better understanding of the biology of their blood supply and pathobiology of angiogenesis [5]. The gold standard for studying the angiogenesis and disease-related vascular aberrations is set by histological examination

Address all correspondence to: Vasilis Ntziachristos, Professor, Chair for Biological Imaging & Institute for Biological and Medical Imaging, Technical University Munich, Munich, Germany, Helmholtz Zentrum München, Deutsches Forschungszentrum für Gesundheit und Umwelt (GmbH), Ingolstädter Landstr., 85764 Neuherberg, Germany.
E-mail: v.natziachristos@tum.de

[1] This work was supported by the EU (European Research Council, ERC-2008-AdG; N233161; MSOT) and by the DFG Cluster of Excellence "Nano-systems Initiative Munich."
[2] Equal contributors.
Received 15 April 2016; Accepted 14 June 2016

1476-5586
http://dx.doi.org/10.1016/j.neo.2016.06.004

of vascularization pattern and density with quantification of branching within the tissue mass, yielding important diagnostic and prognostics data [6]. While specific and highly informative, this method requires biopsy, which not only is susceptible to sampling errors but has limited applications for serial monitoring of tumors [5]. It is also laborious, costly, and offers limited [two-dimensional (2D)] views to the tumors. Thus, there is pressing need in developing cutting-edge technologies for intravital imaging of tumors, which would surpass mentioned methodological limitations and yield three-dimensional (3D) data with precise anatomical registration.

Over the years, X-ray computed tomography and magnetic resonance imaging were applied for vascular imaging *in vivo* and have partly overcome the limitations of the histological method, albeit at higher costs, with lower specificity and occasional inconclusive data and risks of exposure to ionizing radiation or paramagnetic contrast agents [7–9]. Noteworthy, quantification of tumor vascularization using magnetic resonance imaging is also technically challenging, especially for larger vessels, due to poor correlation between magnetic signal and contrast agent concentration as well as erroneous focal enhancement of the signal related to accumulation of the latter [9]. High-resolution optical imaging modalities such as confocal and multiphoton imaging have also been implemented for intravital molecular and functional imaging [10]. The limited field of view along with poor penetration (< 2 mm and < 500 μm, respectively) however renders these inadequate for deep tissue imaging with volumetric measurements of large solid tumors. Recently, multispectral fluorescence ultramicroscopy has been applied for 3D optical sectioning of vascular networks in tumor models, attaining an impressive (6 μm) in-plane resolution, with strong light scattering within the tissue however greatly hampering its *in vivo* applications [11].

Optoacoustic (OA) imaging is an emerging modality of hybrid imaging which utilizes for image production ultrasonic waves generated in response to optical absorption within the tissue exposed to short laser pulses. The capability to resolve the blend and spectra of endogenous and exogenous optical contrast at ultrasonic resolutions has endowed OA imaging the ability to deliver high-resolution readouts from depths not accessible to any other modality of optical microscopy, with tremendous potential for 3D imaging of solid tumors and their vascularization [12–15]. Through combination of single wavelength excitation and raster scanning, OA imaging has been used for visualization of angiogenesis in carcinogenic tissue [16–18]. Optical interferometry with raster scanning at single wavelength excitation has also been applied for monitoring the growth of tumors and their response to therapeutic interventions [19]. Although advantageous, under both arrangements, a single element detector is raster scanned over the area of interest, with hardware limitations imposing major restrictions on multiwavelength excitation and volumetric measurements at high temporal resolution. With implementation of the imaging frequency bandwidth, recently, high-resolution imaging at depths of 2 to 7 mm has been achieved with multispectral optoacoustic mesoscopy (MSOM). We have shown the unique capability of a translate-rotate OA scanner with linear transducer arrays for generating volumetric data sets at mesoscopic scale in acutely excised samples [20] at spatial resolution of ~ 30 μm [21]. The capabilities of this arrangement for 3D volumetric imaging of biological specimens *in vivo* remained to be explored.

Using an innovative arrangement suited for the interrogation of living animals, we implement a translate-rotate scanner for multispectral 3D intravital imaging of the vasculature and hemodynamics of cancerous tumor at a frequency bandwidth of ~ 2 to 40 MHz. We apply MSOM *in vivo* for volumetric measurements of tumor vasculature and showcase high-isotropic-resolution imaging of the entire tumor mass under unperturbed conditions based on endo- and exogenous gold nanoparticles. Finally, we interrogate the distribution of hemoglobin gradients, which suggest constitutive hypoxemia within the tumor core. The findings with MSOM have been confirmed with histology and ultramicroscopic studies of tumors *ex vivo*. The possibility of the future use of MSOM for cancer research is discussed.

Materials and Methods

Experimental Setup and Data Acquisition

Figure 1, *A* and *B* illustrates the experimental setup. Ultrasonic detection was performed using a high-frequency 128-element linear array (Vermon, Tour, France) with a 24-MHz central frequency and an average − 6 dB two-way bandwidth of 60%. The transducer elements had a 70-μm pitch and were cylindrically focused through an acoustic lens at ~ 7.5-mm distance. The recorded signals were digitized by a custom-built data acquisition card (125 M samples/s and 12-bit resolution over a 16-mV range). The linear array was mounted on two motorized stages: a high-accuracy translation stage and a precision rotation stage (M-605.2DD and M-062.PD, respectively, Physik Inst., Karlsruhe, Germany), enabling precise positioning of the transducer and recording of its location (Figure 1*A*). The array was mounted on a custom-made holder, introducing a 45-angular-degree tilt along the elevation dimension. The latter enabled an access for the transducer to the sample under investigation and detection of waves generated by a multitude of absorbers with different orientations, replicating the muddled tumor environment. A custom-made animal holder was designed for mounting the experimental animal. The excitation beam was guided by a 640-fiber bundle partitioned in four arms (Figure 1*B*). The latter were positioned on an arc 1 cm away and oriented toward the sample, enabling optical excitation in a volume of 1 cm^3, optimal for tumor imaging under our settings. Near-infrared excitation light was sourced from a tunable (690-900 nm) optical parametric oscillator laser (OPOTEK, Carlsbad, CA) as nanosecond-long pulses with a 10-Hz repetition rate. The scanning routine used by the OA imaging system was based on the translate-rotate continuous implementation reported previously [18], which was chosen to ensure homogeneous in-plane resolution with good sensitivity to absorbers at all orientations. The linear array was continuously rotated 172° around the sample at a predefined speed, which was selected based on the repetition rate of the pulsed laser. For each laser shot, a trail of recording was transferred to the data acquisition system (DAQ) and digitized. The radius of the transducer's middle element (64) was set at 6.3 mm and corresponded with the middle plane of the experimental specimen. For tumor visualization, animals were placed on the bed holder, exposing the tumor mass regions through an aperture of the holder and enabling its direct contact with preheated water used as an acoustic coupling medium (Figure 1*B*).

Phantom and Animal Preparations

System characterization was performed on three turbid phantoms made of 1.6% agar and 0.8% intralipid (Sigma Aldrich, Germany), which were molded to form a cylindrical shape, in a 5-ml syringe (Figure 2). The molds measured 11 mm in diameter and 2 cm in

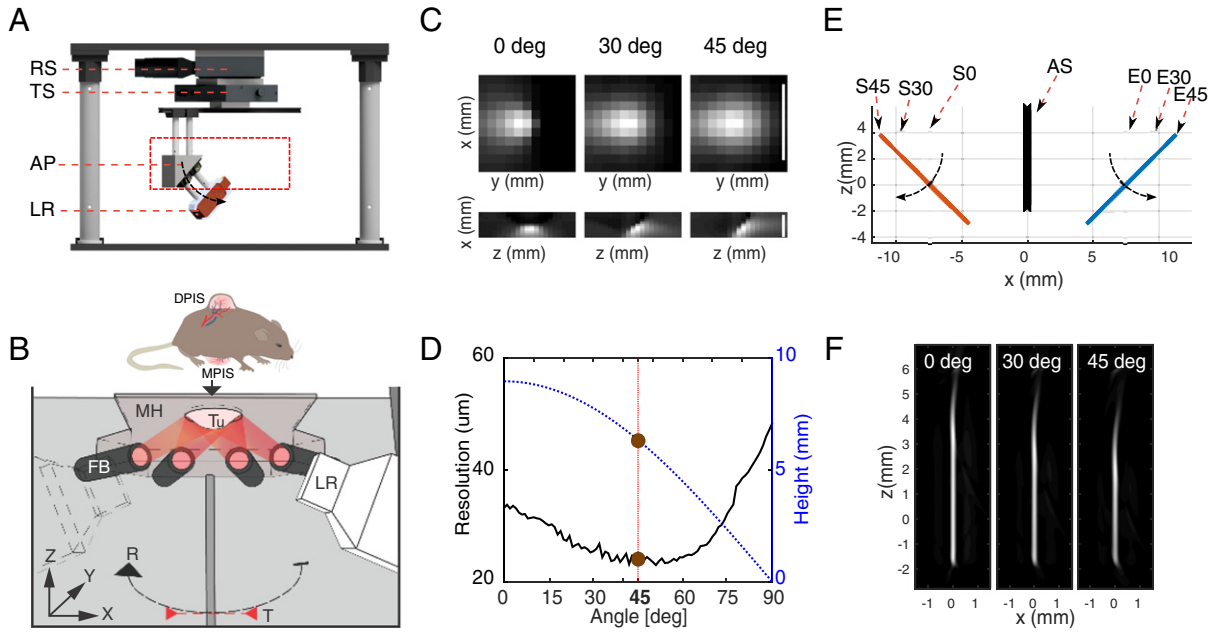

Figure 1. An overview of the experimental setup and data simulation. (A) Experimental setup: linear array mounted on a high-precision translation stage, attached to a rotation platform. The transducer is connected to a specially designed holder, tilting the length axis to 45 angular degrees, providing access to the sample under investigation. *RS*, rotation stage; *TS*, translation stage; *AP*, adapting plate; *LR*, linear array. (B) Schematic of the implantation sites of tumors in a mouse (top) with a view of the mouse holder (MH) and the four fiber bundles (FB) delivering the illumination to the tumor (Tu) (bottom). Arrow with dashed line indicates the rotation trajectory of the linear array, while red arrowheads depict the translation motion. (C) Simulated results of 10-μm microspheres with different tilting angles of the transducer (0°, 30°, and 45°): an aerial view (*xy* plane) and side view (*xz* plane). (D) Graphical representation of the relationship between the encompassed volume of the sample and angular tilting of the array (blue dashed curve) and standard deviation of the 3D resolution (black curve). (E, F) Simulated configuration of a center absorber (suture; 100-μm diameter) with the first (red) and last (blue) detector positions in a tomographic scan varying the angular tilting of the transducer with reconstructed images along the *xz* plane depicting the absorber for 0°, 30°, and 45° tilting of the array. *AS*, absorbing suture; *S*, starting; *E*, ending degrees.

height. Phantom 1 was comprised of a 30-µm–diameter black polyamide suture (Vetsuture, Paris, France) arranged in a single 1-cm–long knot, which was placed vertically in the embedding medium to mimic an absorbing sample with a complex shape of different absorber orientations. Phantom 2 contained 9 microspheres (D = 200 µm; Cospheric LLC, Santa, Barbara, CA) arranged to form a "plus" shape along the entire diameter of the embedding medium (1 cm) and was used to characterize the in-plane field of view of the system. Phantom 3 was made of 10-µm microspheres (Polybead Microspheres; Polysciences, Inc., Warrington, PA) diluted in agar and spread across a 1-cm^3 area to provide a reference for computing the resolution of the system with respect to isotropic absorbers generating broadband frequencies.

The *in vivo* experiments were performed on 8-week-old athymic nude-Foxn1 female mice (Harlan, Germany) implanted subcutaneously or orthotopic with 4T1 carcinoma (breast tumor

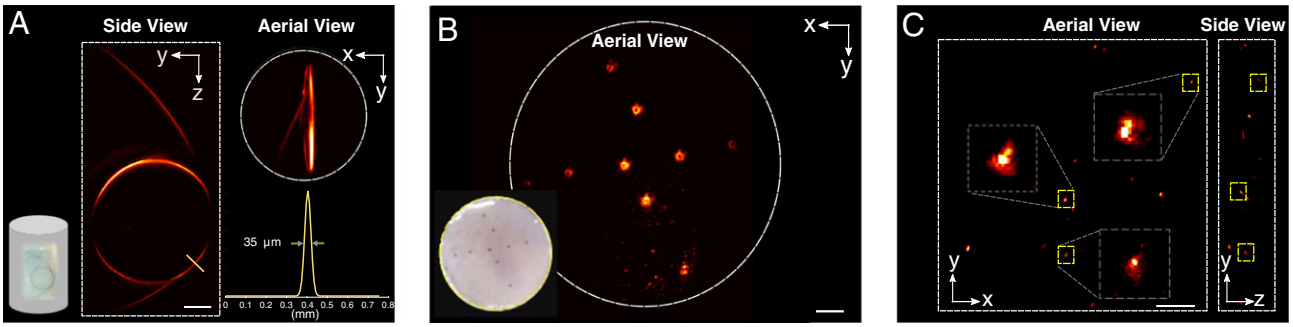

Figure 2. Characterization of the performance of the MSOM in phantoms. (A) Phantom 1 (left inset, an overview): OA view of 30-μm knot suture—maximum intensity projection (MIP) side view (left) and aerial view (right, top). Inset (yellow) represents an intensity profile of the 30-μm suture. (B) Phantom 2 (left inset, an overview): 9 microspheres (200-μm diameter each) scattered over the surface of the cylindrical mold—MIP aerial view. (C) Phantom 3: 10-μm microspheres—MIP; aerial and side views. Boxed: microspheres presented at higher magnification. Scale bar: 1 cm.

model). The first animal (mouse 1) was inoculated with cell suspensions in the dorsal upper pelvis (1 million 4T1), while the second (mouse 2) received orthotopic implant into the mammary pad (0.5 million 4T1 cells) (CRL-2539). Imaging procedures were performed under general anesthesia (1.8% isoflurane with 100% O_2) and have been approved by the Government of Upper Bavaria (N 55.2.1.54-2632-102-11). Cells were authenticated by the ACTT postfreeze viability, morphology, mycoplasma contamination, growth, and interspecies determination tests as well as bacterial and fungal contamination, with all tests proven to be negative. Imaging was started after tumors reached ~1 cm^3; mouse 1 was imaged 10 days after inoculation with single wavelength optical excitation, while mouse 2 was imaged 11 days after tumor inoculation and 1 hour after intravenal injection of gold nanoparticles (50 μl of gold nanoparticles, equivalent to 6e10 particles/μl). For spectral imaging, multispectral acquisitions between 720 and 815 nm were performed. The averaged laser power was tested before each scan with a power meter FieldMaxII-Top (Coherent, Santa Clara, CA) to correct for its fluctuations in the course of experiment.

Histochemical Staining of Cancerous Tissue and Ultramicroscopic Analysis

Histochemical staining and ultramicroscopic analysis have been implemented for postmortem validation of the cancerous tissue *ex vivo*, with experimental procedures and results detailed in the Supplementary Methods and Results.

Data Processing and Analysis

Noise filtering was performed off-line based on the transducer specifications. Signals were band-pass (2-40 MHz) filtered with Butterworth (order 3). A wavelet decomposition (db2) with two levels of discrimination was performed on filtered signals to separate the data into low- and high-frequency components. The two decomposed levels were separately reconstructed using a 3D filtered back-projection algorithm [19]. The reconstructed volumetric data sets were loaded in Amira (FEI, Visualization Sciences Group, Germany) with visualization angles selected for volumetric rendering and illustration purpose. The two wavelet-decomposed images were superimposed using ImageJ. Spectral unmixing was applied to detect the presence of oxygenated or deoxygenated hemoglobin or injected contrast agent. Before unmixing, multispectral images were corrected for wavelength-dependent fluctuations of the laser power. For each reconstructed voxel, the absorbed spectrum within this voxel was fitted linearly with that of the expected components present in the sample. Four known spectra corresponding to deoxy- and oxyhemoglobin (HbO_2 and Hb), the injected nanorods, and a constant spectrum were used for unmixing process and background normalization.

Results

Design and Conceptual Validation of the Experimental Setup

To achieve *in vivo* volumetric visualization of solid tumors, a new imaging principle has been implemented based on the previously reported translate-rotate detection geometry [21]. Advantage has been taken from optimizing imaging perspective of the linear array scanner, generating a conical detection surface, which enabled application of MSOM for imaging of solid tumors *in vivo* (Figure 1, *A* and *B*). The operational capabilities of the system have been assessed using analytical simulations of 10-μm absorber placed in the center of the coordinate system. An incremental inclination angle was used in order to compute 91 reconstructed volumes. Figure 1*C* presents results gained from simulated absorber at three different angular tilting values. Although changes in the angle of the transducer array did not visibly alter the in-plane *xy* resolution, improvements have been achieved in *z* dimension. Indeed, in conical configuration of imaging, the elongation of the absorber (Figure 1*C*) along the vertical axis is notably reduced compared to the cylindrical implementation ("rice-grain" aspect in *xz* plane 0° tilting of the array). Figure 1*D* depicts a plot (black line) of the standard deviation of the resolution values along the *x*, *y*, and *z* dimensions for the simulated absorber at all 91 angular positions. As can be seen, at 45° inclination, the standard deviation is relatively reduced (~25 μm), implying an isotropic resolution. Moreover, by calculating the volumetric aperture of the system, the sampling volume was measured to be 6.34 mm in height (blue dotted line). A further assessment of the sampling volume by tilting the angle of the transducer has confirmed the predicted reduction of the vertical aperture of the system (Figure 1, *E* and *F*). Using an absorbing suture (100 μm in diameter), a clear decrease in vertical field of view has been also verified with such an arrangement.

Characterization of the Performance of MSOM System

The volumetric capabilities of the MSOM system for visualization of multiple orientations of the specimen were characterized using phantom 1, with results presented in Figure 2*A*. The composite shape of a 30-μm–diameter single-looped knot of the suture provides a model multifaceted structure, which was imaged and serially reconstructed over the entire volume, scaling 9 mm in height and 10 × 10 mm along *xy* planes. The aerial view of maximum intensity projection (MIP) of the reconstructed volume shows the circular pattern of the single-looped knot. As evident, the reconstructed volume does not reveal any elongations along any axis, implying resolution homogeneity of the entire field of view. To confirm that 3D reconstructed images can be quantified, an intensity profile across one side of the suture was computed and full width at half maximum was defined (Figure 2*A*). To evaluate the imaging field of view of MSOM, phantom 2 comprised of 9 microspheres of 200 μm in diameter was scanned. The microspheres were arranged to form a "plus" sign along the surface of the phantom (Materials and Methods). Figure 2*B* represents the reconstructed MIP along the *z* axis. As evident, the microspheres can be clearly resolved along the entire diameter of the sample, with dust particles also visible on the lower part of the reconstructed volume. Likewise, phantom 3 comprised of microspheres of 10 μm diameter and randomly scattered within the content of the agar was imaged to determine the resolution of the system with respect to isotropic objects. Three microspheres located at different depths and random in-plane positions were selected for full width at half maximum computation based on their intensity profile (Figure 2*C*). The estimated resolution derived from these measurements is close to 70 μm along all tested dimensions. Collectively, these data are in agreement with previous OA measurements with the use of the same transducer and confirm that the MSOM system achieves an isotropic resolution along the *x*, *y*, and *z* dimensions and thus is suitable for volumetric imaging of biological samples.

Volumetric Imaging of the Vasculature of Cancerous Tissue In Vivo

A subcutaneous 4T1 tumor model was selected for imaging the vasculature inside the cancerous tissue mass, based on the intrinsic optical contrast, on day 10 postinoculation (mouse 1) *in vivo*.

Figure 3, *A* and *B* depicts a subcutaneous tumor implant (~9 mm in diameter) in the dorsal upper pelvis prior to OA imaging. The apparent hyperemia with rubor indicates local immune response with intense metabolism of proliferating tissue. The OA view of the tissue mass reveals its profuse vascularization with dense network of vessels of varying diameters, as coded with color (Figure 3*C*). Of note, the microvessels appear to concentrate at the periphery, while the larger vessels with profuse anastomoses feed the deeper compartments of the cancerous tissue mass. To obtain a volumetric view of the tumor, volume-rendered 3D single-wavelength (760 nm) images were acquired and reconstructed with Amira. Assessments of the diameter of the randomly selected vessels on the maximal area projection revealed a range of diameters varying between 70 μm and 250 μm, with microvessels clearly distinguishable on the surface as well as deep inside of the tumor. Optoacoustic 2D cross-sectioning of the tissue mass revealed asymmetric distribution of the vasculature, with prevalence of dense networks of anastomosis at the base of the tumor, while the core and apex receive a more refined system of blood supply (Figure 3, *E*–*G*). To evaluate the utility of MSOM for fine vascular morphometry and assessment of the vessel diameter and branching, two regions of interest were visualized at higher magnification (Figure 3, *F* and *G*). As evident, this approach enables measurements of the vessel diameter on randomly defined segments along with intensity profile and confirms the applicability of intravital MSOM imaging for resolving both large vessels and microvasculature within tumors, essential for studies of the biology and pathobiology of vascularization of the solid tumor tissue. Thus, based on the endogenous contrast, profuse vascularization of the tissue mass with large and small vessels can be volumetrically visualized and analyzed. Importantly, as shown in Figure 3, both 2D and 3D projections can be selected for closer examination of the vascular elements of the tumor to reveal greater morphological details at different depths of the tissue mass.

Application of MSOM for Nanoparticle and Functional Imaging of Tumors

To confirm the utility of MSOM as a versatile tool for volumetric imaging of solid tumors with endo- and exogenous contrast as well as

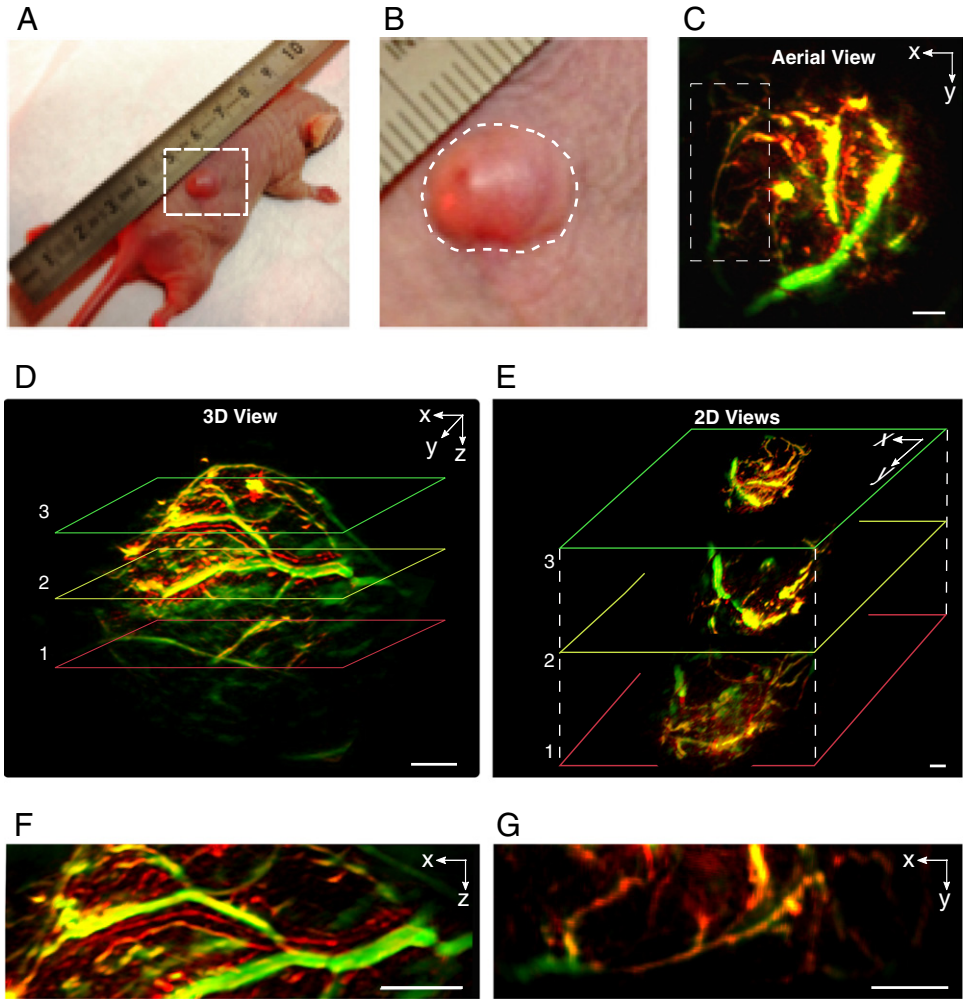

Figure 3. Label-free intravital imaging of the tumor vasculature of subcutaneous 4T1 tumor with MSOM. (A) Color photograph of the mouse model (mouse 1; day 11 postinoculation). (B) Higher-magnification photograph of the tumor site: the body of the tumor marked with dashed line. (C) MSOM image representing MIP of the entire tumor: aerial view. (D, E) Volume-rendered image of the tumor with highlighted three (1-3) cross sections (D) and planar view of individual planes corresponding to different depths of imaging (E). Visualization of three 2D vertical (z) positions selected from top, middle, and bottom of the tumor mass. (F, G) Magnified view of the vascular network and branching within the core of the tumor and at the periphery. Scale bar: 1 cm.

functional measurements, an orthotopic 4T1 breast tumor implant in the mammary pad of a mouse (mouse 2) was scanned on day 11 postinoculation. Gold nanoparticles were used as an exogenous contrast, while O_2-related spectral changes in the hemoglobin absorbance were taken as indicative of the oxygenation levels across the cancerous mass. Figure 4, *A* and *C* illustrates an overview of the orthotopic 4T1 tumor with MSOM image of the reconstructed vasculature. Similar to the subcutaneous tumor (mouse 1), the mammary implant measured ~9 mm in diameter and revealed signs of local inflammation and enhanced metabolic activity with profuse system of vascularization (Figure 4*A*). Spectral comparison of the hemoglobin saturation across the tumor mass revealed markedly lower oxygenation within the tumor core, in line with previous reports [22,23] (Figure 4*D*). Imaging of the tumor 1 hour after intravenous injection of gold nanoparticles demonstrates exquisite labeling with strong contrast of the vasculature and their ready transfusion throughout the entire tumor volume, including its core (Figure 4*E*).

To verify revealed by MSOM histologically abnormalities of the morphology of tumor vascularization, postmortem ultramicroscopy and histochemical assessments have been carried out. After MSOM imaging, under deep anesthesia, mouse was injected with Lectin-InvivoTag 750 (2 nmol/0.5 ml, i.v.) and killed with ketamine overdose (120 mg/kg). Tumor was excised, processed for ultramicroscopy with hematoxylin and eosin staining, and imaged. Distinct

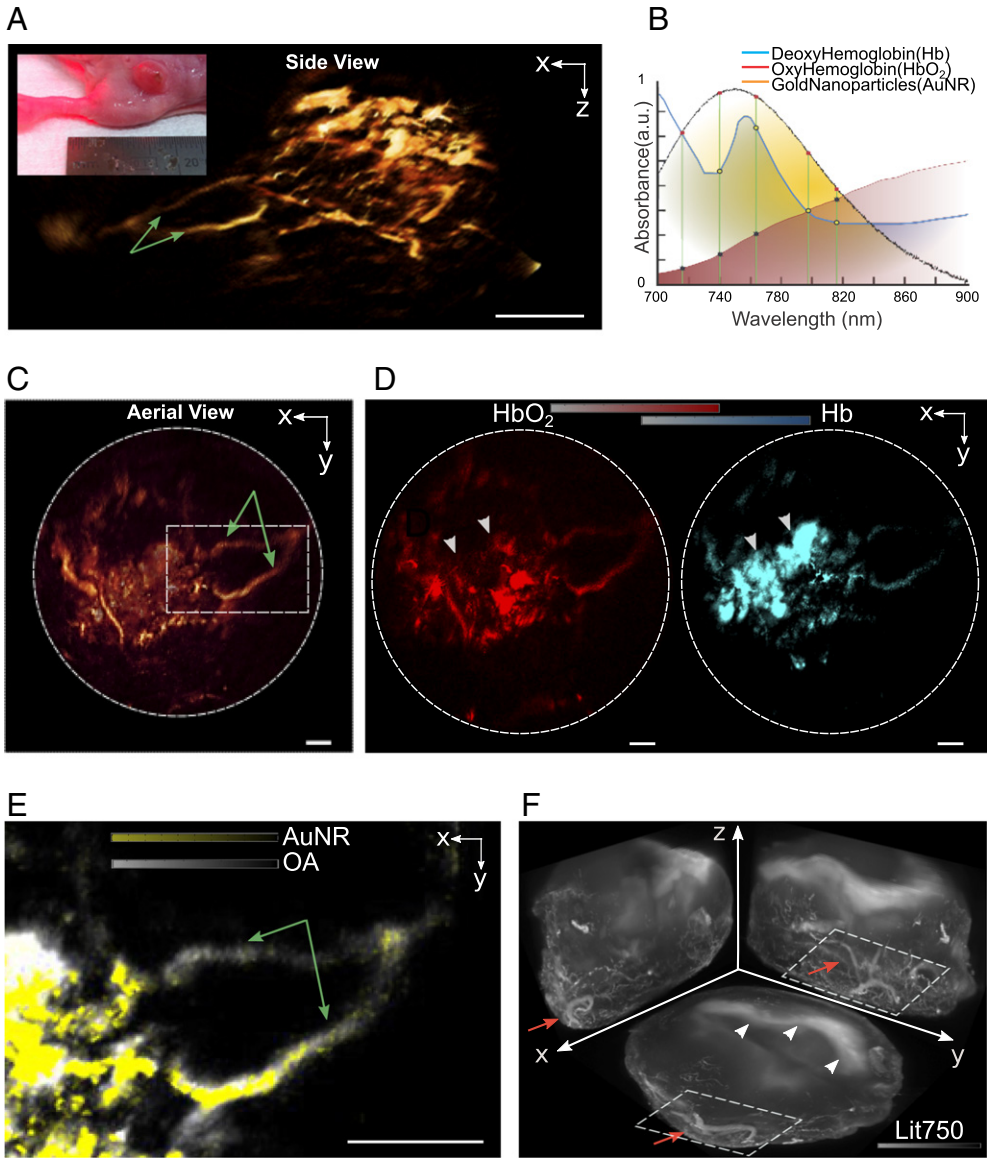

Figure 4. Structural, functional, and molecular MSOM of a 4T1 orthotopic (mouse 2; day 11) tumor *in vivo*. (A) Optoacoustic image of a 4T1 orthotopic tumor (side view) with color photograph of the mouse with mammary implant (inset, left). (B) Graphical representation of the absorption spectra of the extrinsic agent (gold nanoparticles, AuNR) and of the oxy- and deoxyhemoglobin (Hb and HbO_2, respectively). (C) Optoacoustic aerial view of the tumor (from A) and (D) color-coded images of the distribution of the HbO_2 and Hb within the core of the tumor: an aerial view. Double white arrows highlight differential distribution of the HbO_2 and Hb. (E) Magnified view of in-boxed region (C) with vascular labeling using gold nanorods (yellow). (F) 3D MIP projections of ultramicroscopy showing vascular tagging with Lectin-InvivoTag 750. White arrows point to aggregates of fibrin with necrotic tumor cells within the core (see also Figure 5*A*). Scale bar: 1 cm.

labeling of the vasculature with Lectin-InvivoTag 750 is clearly visible through the red channel, while autofluorescence marking the stroma and contours of the tumor is visible in green (Figures 4*F* and 5, *B* and *C*). Of note, Lectin-InvivoTag 750 staining of the core of the tumor was sparse, suggestive of a deep necrotic process within the tissue mass (Figure 4*F*). The later was confirmed also by histological examination (Figure 5*A*). At this stage, however, we cannot rule out the contribution of the poor penetration of Lectin-InvivoTag 750 into the core of the tumor. Overall, these data confirm the applicability of MSOM as a versatile tool for visualization and volumetric studies of solid tumors *in vivo*, with readouts compatible to those obtained through more invasive histochemical methods combined with microscopy.

Discussion

Understanding the mechanisms governing the angiogenesis and vascularization of solid tumors *in vivo* is of major basic and translational importance, with direct diagnostic and prognostic implications [2–4]. Available means for angiography and imaging the vascularization of tumors, while informative, also have major limitations, demanding their further improvement with better characterization. OA imaging emerges as a powerful bioimaging modality and has been applied for basic and preclinical studies of tumors and tumor-related angiogenesis *in vivo* [22,24–26]. These, however, provided limited information of the exquisite morphology and architecture of the vascularization and were specialized for capturing general features of solid tumors [14]. To reveal a fuller picture and gain better in-depth resolution, we have implemented recently a raster scanning approach [17]. Improved spatial resolution and image quality reported in this study, however, came with restriction to a single wavelength optical excitation, lower data acquisition rate, and limited access [16,18,19,27]. To gain spectral information, optical interferometry with multiple wavelength excitations has been implemented for imaging tumor growth and treatment response over time [19,28]. We have recently applied a spherical ultrasound detection array for real-time vascular imaging with functional and structural capabilities, albeit with limited spatial resolution and poor feature imagining capacities [29]. Taking these into consideration, herein we introduce a novel translate-rotate detector-based MSOM system for multispectral volumetric mesoscopy of solid tumors with improved accessibility. A linear high-frequency transducer has been combined with a flexible arrangement of detectors to capture the entire tumor mass (1 cm^3) at a uniform spatial resolution of ~70 μm and improved feature representation. Proof of principle is provided for the applicability of high-resolution imaging toward tracking systemically applied contrast as well as visualization of hemoglobin gradients, which are of prime relevance to pharmacokinetics, drug penetration, and metabolic rate studies. Overall, these advances extend the OA mesoscopy toward improved lateral and axial resolution with volumetric imaging capabilities.

The performance of MSOM system has been tested in two models of solid malignant tumors: subcutaneous and orthotopic implants, followed by postmortem histochemical analysis. It is important to note that, in addition to proving the general feasibility of the volumetric mesoscopy of tumors, the orthotopic mammary implants studied herein provide a realistic model for pre-clinical breast cancer research [30]. Encouragingly, the overall topography and distribution of the vasculature within the tumor mass revealed with MSOM are in agreement with our histological data as well as with results of ultramicroscopic analysis, demonstrating dense vascularization of the stroma of the tumor with irregularly branching vessels of tortuous shape and profuse anastomoses and lacunas, considered as hallmarks of malignant cancers [31–33]. The latter are likely to contribute toward irregular blood flow with low oxygenation levels in the core of the growing tissue mass, along with signs of local immune response, as evident from hyperemia seen in our models. Interestingly, reports indicate that the nascent vascular system within solid tumors is represented by endothelial cell tubes, which lack well-developed wall structures and exhibit a limited capacity for blood flow with gas and nutrient exchange [34–36]. These observations are in agreement with preclinical and clinical data, showing a similar histopathological profile in breast cancer models and human samples [37,38]. The capability of MSOM to resolve the fine contrasts provided by nanoparticle as well as map hemoglobin gradients [26,39,40] implies its suitability as a tool for quantifying of hemodynamics and diffusion

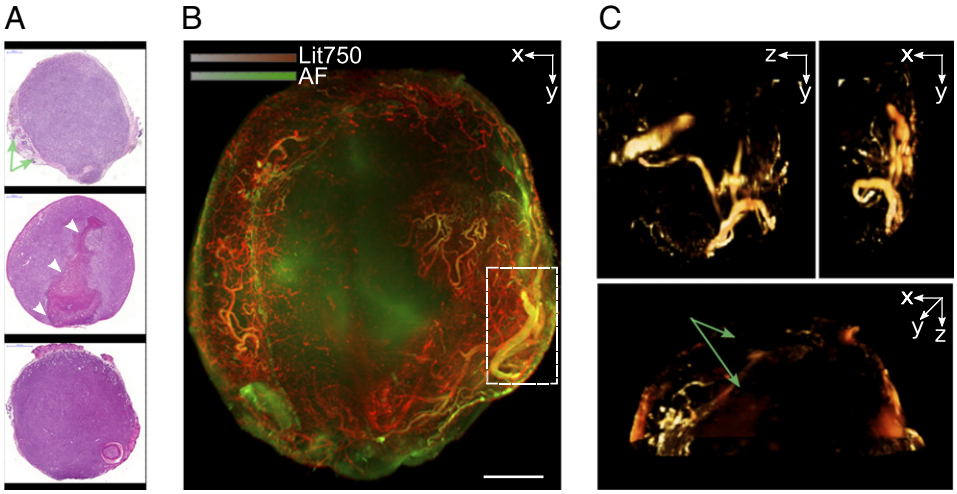

Figure 5. (A) 2D histological cross sections (Hematoxylin Eosin - H&E) of a tumor corresponding to three planes selected at different depths. (B) MIP view of ultramicroscopic reconstruction of the tumor: autofluorescence—green; lectin vascular labeling—red with inboxed area presented at higher magnification in (C). Note the tortoise appearance of the major vasculature within the core of the tumor. Scale bar: 1 cm.

of the materials within solid tumors *in vivo* with high specificity and sensitivity, advocating its broad future applications.

From a technical point of view, by combining high-resolution multispectral imaging with improved accessibility and enhanced data acquisition rates, the technology presented herein makes a substantial step forward compared to other optical intravital vascular imaging modalities. The implemented flexible scanning geometry facilitates a broad coverage angle with true volumetric recordings of the OA signals generated deep within the tissue. This feature constitutes a principal advantage over previously presented systems with a single element detector with limited access to the sample and poor 3D imaging capabilities. In regard to longitudinal studies, compared to systems with only cross-sectional imaging capabilities, MSOM described here offers full-view visualization of the entire sample, eliminating the need in challenging histological procedure of reproducing the same plane for imaging. A similar translate-rotate platform was used earlier to extract anatomical and functional information from excised samples, but due to the enclosed angle imposed in cylindrical configuration, the sample under investigation could not measure more than 12 mm [41]. By including an inclination angle of the transducer along the long axis, in this study, a conical detection surface has been generated, which enables a larger interrogation field with an isotropic volumetric imaging. Implementation of the translate-rotate geometry as shown, thus, introduces an optimal balance between the field of view necessary for intravital imaging and 3D resolution performance, never reported previously. From a detection point of view, the MSOM system presented herein affords recordings in higher frequency ranges, gaining better resolutions with higher tolerance to the depth-related corruption of ultrasound signals. Finally and complementarily, the versatility of the approach used herein enables imaging of wide ranges of configurations with broader choice of research models.

Although at present the temporal resolution of MSOM is limited by the repetition rate of the pulsed laser, research is currently under way toward overcoming this constraint. Increased pulse repetition would afford several benefits, including monitoring faster biological and physiological processes. Improved spatial and temporal resolution together with multispectral capabilities should also be beneficial for future studies of vascularization and functional dynamics of tumors and other neoplasia, facilitating the research and understanding of the pathobiology of angiogenesis in murine tumor models, with implication for oncology and oncotherapy.

Acknowledgements

This work was supported by the EU (European Research Council, ERC-2008-AdG; N233161; MSOT) and by the DFG Cluster of Excellence "Nano-systems Initiative Munich." The authors wish to acknowledge Uwe Klemm and Sarah Glasl for their valuable technical support on animal handling.

Appendix A. Supplementary data

Supplementary data to this article can be found online at http://dx.doi.org/10.1016/j.neo.2016.06.004.

References

[1] Jain RK (1988). Determinants of tumor blood flow: a review. *Cancer Res* **48**(10), 2641–2658.

[2] Bergers G and Benjamin LE (2003). Tumorigenesis and the angiogenic switch. *Nat Rev Cancer* **3**(6), 401–410.

[3] Heijblom M, Klaase JM, van den Engh FM, van Leeuwen TG, Steenbergen W, and Manohar S (2011). Imaging tumor vascularization for detection and diagnosis of breast cancer. *Technol Cancer Res Treat* **10**(6), 607–623.

[4] Carmeliet P and Jain RK (2000). Angiogenesis in cancer and other diseases. *Nature* **407**(6801), 249–257.

[5] McDonald DM and Choyke PL (2003). Imaging of angiogenesis: from microscope to clinic. *Nat Med* **9**(6), 713–725.

[6] Nico B, Benagiano V, Mangieri D, Maruotti N, Vacca A, and Ribatti D (2008.). Evaluation of microvascular density in tumors, pro and contra; 2008.

[7] Kim SH, Kamaya A, and Willmann JK (2014). CT perfusion of the liver: principles and applications in oncology. *Radiology* **272**(2), 322–344.

[8] Kiessling F, Greschus S, Lichy MP, Bock M, Fink C, Vosseler S, Moll J, Mueller MM, Fusenig NE, and Traupe H, et al (2004). Volumetric computed tomography (VCT): a new technology for noninvasive, high-resolution monitoring of tumor angiogenesis. *Nat Med* **10**(10), 1133–1138.

[9] Jeswani T and Padhani AR (2005). Imaging tumour angiogenesis. *Cancer Imaging* **5**(1), 131–138.

[10] Kedrin D, Gligorijevic B, Wyckoff J, Verkhusha VV, Condeelis J, Segall JE, and van Rheenen J (2008). Intravital imaging of metastatic behavior through a mammary imaging window. *Nat Methods* **5**(12), 1019–1021.

[11] Dobosz M, Ntziachristos V, Scheuer W, and Strobel S, et al (2014). Multispectral fluorescence ultramicroscopy: three-dimensional visualization and automatic quantification of tumor morphology, drug penetration, and antiangiogenic treatment response. *Neoplasia* **16**(1), 1–13.

[12] Ntziachristos V (2010). Going deeper than microscopy: the optical imaging frontier in biology. *Nat Methods* **7**(8), 603–614.

[13] Wang LV and Hu S (2012). Photoacoustic tomography: in vivo imaging from organelles to organs. *Science* **335**(6075), 1458–1462.

[14] Taruttis A, van Dam GM, and Ntziachristos V (2015). Mesoscopic and macroscopic optoacoustic imaging of cancer. *Cancer Res* **75**(8), 1548–1559.

[15] Taruttis A and Ntziachristos V (2015). Advances in real-time multispectral optoacoustic imaging and its applications. *Nat Photonics* **9**(4), 219–227.

[16] Siphanto R, Thumma KK, Kolkman RGM, Van Leeuwen TG, De Mul FFM, Van Neck JW, Van Adrichem LNA, and Steenbergen W (2005). Serial noninvasive photoacoustic imaging of neovascularization in tumor angiogenesis. *Opt Express* **13**(1), 89–95.

[17] Omar M, Schwarz M, Soliman D, Symvoulidis P, and Ntziachristos V (2015). Pushing the optical imaging limits of cancer with multi-frequency-band raster-scan optoacoustic mesoscopy (RSOM). *Neoplasia* **17**(2), 208–214.

[18] Lao Y, Xing D, Yang S, and Xiang L (2008). Noninvasive photoacoustic imaging of the developing vasculature during early tumor growth. *Phys Med Biol* **53**(15), 4203–4212.

[19] Laufer J, et al (2012). In vivo preclinical photoacoustic imaging of tumor vasculature development and therapy. *J Biomed Opt* **17**(5), 056016-1–056016-8.

[20] Gateau J, Chekkoury A, and Ntziachristos V (2013). Ultra-wideband three-dimensional optoacoustic tomography. *Opt Lett* **38**(22), 4671–4674.

[21] Chekkoury A, Gateau J, Driessen W, Symvoulidis P, Beziere N, Feuchtinger A, Walch A, and Ntziachristos V (2015). Optical mesoscopy without the scatter: broadband multispectral optoacoustic mesoscopy. *Biomed Opt Express* **6**(9), 3134–3148.

[22] Herzog E, Taruttis A, Beziere N, Lutich AA, Razansky D, and Ntziachristos V (2012). Optical imaging of cancer heterogeneity with multispectral optoacoustic tomography. *Radiology* **263**(2), 461–468.

[23] Beziere N, Lozano N, Nunes A, Salichs J, Queiros D, Kostarelos K, and Ntziachristos V (2015). Dynamic imaging of PEGylated indocyanine green (ICG) liposomes within the tumor microenvironment using multi-spectral optoacoustic tomography (MSOT). *Biomaterials* **37**, 415–424.

[24] Li M, Oh JT, Xie X, Ku G, Wang W, Li C, Lungu G, Stoica G, and Wang LV (2008). Simultaneous molecular and hypoxia imaging of brain tumors in vivo using spectroscopic photoacoustic tomography. *Proc IEEE* **96**(3), 481–489.

[25] Lungu GF, Li ML, Xie X, Wang LV, and Stoica G (2007). In vivo imaging and characterization of hypoxia-induced neovascularization and tumor invasion. *Int J Oncol* **30**(1), 45–54.

[26] Mallidi S, Kim S, Karpiouk A, Joshi PP, Sokolov K, and Emelianov S (2015). Visualization of molecular composition and functionality of cancer cells using nanoparticle-augmented ultrasound-guided photoacoustics. *Photoacoustics* **3**(1), 26–34.

[27] Laufer J, Jathoul A, Johnson P, Zhang E, Lythgoe M, Pedley RB, Pule M, and Beard P (2012). In vivo photoacoustic imaging of tyrosinase expressing tumours in mice. SPIE BiOS. International Society for Optics and Photonics; 2012.

[28] Jathoul AP, Laufer J, Ogunlade O, Treeby B, Cox B, Zhang E, Johnson P, Pizzey AR, Philip B, and Marafioti T, et al (2015). Deep in vivo photoacoustic imaging of mammalian tissues using a tyrosinase-based genetic reporter. *Nat Photonics.* **9**, 239–246

[29] Ermolayev V, Dean-Ben XL, Mandal S, Ntziachristos V, and Razansky D (2015). Simultaneous visualization of tumour oxygenation, neovascularization and contrast agent perfusion by real-time three-dimensional optoacoustic tomography. *Eur Radiol.* **26**(6), 1843–1851

[30] Kubota T (1994). Metastatic models of human cancer xenografted in the nude mouse: the importance of orthotopic transplantation. *J Cell Biochem* **56**(1), 4–8.

[31] Baish JW and Jain RK (2000). Fractals and cancer. *Cancer Res* **60**(14), 3683–3688.

[32] Baluk P, Hashizume H, and McDonald DM (2005). Cellular abnormalities of blood vessels as targets in cancer. *Curr Opin Genet Dev* **15**(1), 102–111.

[33] Hanahan D and Weinberg RA (2011). Hallmarks of cancer: the next generation. *Cell* **144**(5), 646–674.

[34] Carmeliet P and Jain RK (2011). Principles and mechanisms of vessel normalization for cancer and other angiogenic diseases. *Nat Rev Drug Discov* **10**(6), 417–427.

[35] Vaupel P, Kallinowski F, and Okunieff P (1989). Blood flow, oxygen and nutrient supply, and metabolic microenvironment of human tumors: a review. *Cancer Res* **49**(23), 6449–6465.

[36] Jain RK (2008). Taming vessels to treat cancer. *Sci Am* **18**, 64–71.

[37] Pulaski BA and Ostrand-Rosenberg S (2001). Mouse 4T1 Breast Tumor Model. Current Protocols in Immunology. John Wiley & Sons, Inc.; 2001.

[38] Prewett M, Huber J, Li Y, Santiago A, O'Connor W, King K, Overholser J, Hooper A, Pytowski B, and Witte L, et al (1999). Antivascular endothelial growth factor receptor (fetal liver kinase 1) monoclonal antibody inhibits tumor angiogenesis and growth of several mouse and human tumors. *Cancer Res* **59**(20), 5209–5218.

[39] Liopo A, Su R, and Oraevsky AA (2015). Melanin nanoparticles as a novel contrast agent for optoacoustic tomography. *Photoacoustics* **3**(1), 35–43.

[40] Ntziachristos V and Chance B (2000). Breast imaging technology: probing physiology and molecular function using optical imaging—applications to breast cancer. *Breast Cancer Res* **3**(1), 3–41.

[41] Gateau J, Chekkoury A, and Ntziachristos V (2013). High-resolution optoacoustic mesoscopy with a 24 MHz multidetector translate-rotate scanner. *J Biomed Opt* **18**(10), 106005:1–10.